CrossMark

The Influence of Spray Parameters on the Characteristics of Hydroxyapatite In-Flight Particles, Splats and Coatings by Micro-plasma Spraying

Xiao-mei Liu[1] · Ding-yong He[1,2] · Yi-ming Wang[1] · Zheng Zhou[1,2] ·
Guo-hong Wang[2] · Zhen Tan[1] · Zeng-jie Wang[2]

Abstract Hydroxyapatite (HA) is one of the most important bioceramic materials used in medical implants. The structure of HA coatings is closely related to their manufacturing process. In the present study, HA coatings were deposited on Ti-6Al-4V substrate by micro-plasma spraying. Results show that three distinct HA coatings could be obtained by changing the spraying power from 0.5 to 1.0 kW and spraying stand-off distance from 60 to 110 mm: (1) high crystallinity (93.3%) coatings with porous structure, (2) high crystallinity coatings (86%) with columnar structure, (3) higher amorphous calcium phosphate (ACP, 50%) coatings with dense structure. The in-flight particles melting state and splat topography was analyzed to better understand the formation mechanism of three distinct HA coatings. Results show that HA coatings sprayed at low spraying power and short stand-off distance exhibit high crystallinity and porosity is attributed to the presence of partially melted particles. High crystallinity HA coatings with (002) crystallographic texture could be deposited due to the complete melting of the in-flight particles and low cooling rate of the disk shape splats under

higher spraying power and shorter SOD. However, splashed shape splats with relative high cooling can be provided by increasing SOD, which leads to the formation of ACP.

Keywords hydroxyapatite coatings · micro-plasma spraying · in-flight particles · texture

Introduction

Hydroxyapatite (HA) is one of the most important bioceramic materials used in a medical implants because it has excellent biocompatibility and osteoconductivity, allowing bone cells to grow on its surface (Ref 1-3). It has been used successfully in biomedical implant material for many years, such as tooth, knee and hip replacement. However, HA has poor bending strength and fracture toughness and is therefore unsuitable for use in implants under shear loading. For this reason, HA is deposited on metal material, such as titanium, magnesium, and stainless steel, which can provide higher strength and fracture toughness. Various methods have been used in the production of HA coatings, such as thermal spraying techniques (Ref 4-6), chemical vapor deposition (CVD) technique (Ref 7, 8), physical vapor deposition (PVD) (Ref 9-15), electrophoretic deposition (EPD) technique (Ref 16-20), sol–gel technique (Ref 21, 22), and so forth. Among the various deposition techniques, the thermal spraying process, especially atmospheric plasma spraying (APS) (Ref 4-6), vacuum plasma spraying (Ref 23-25) and high velocity oxy-fuel (HVOF) spraying (Ref 26-28), is the most popular method to deposit HA coating. Due to the advantages that include high coating adhesion and high deposition efficiency, plasma spraying has been widely used to deposit HA coatings on

✉ Xiao-mei Liu
liuxiaomei@emails.bjut.edu.cn

✉ Ding-yong He
dyhe@bjut.edu.cn

1 College of Materials Science and Engineering, Beijing University of Technology, Beijing, China

2 Beijing Engineering Research Center of Eco-Materials and LCA (Beijing University of Technology), Beijing, China

metallic implants surface (Ref 29, 30). However, it was reported that the high temperature of plasma jet could lead to decomposition phases, such as tricalcium phosphate (TCP) and amorphous calcium phosphates (ACP). Crystalline HA is very stable in the physiological fluids, but the TCP and the ACP have higher dissolution rates, and the dissolution of those phases is harmful for the long-term reliability of the implants (Ref 31). Therefore, being highly crystallinity and phase pure is pursued for the long-term stability of HA coating. Compared with traditional plasma spraying, micro-plasma spraying requires much less power (1-4 kW) and can be used to prepare HA coatings with higher degree of crystallinity (> 90%). Moreover, MPS can produce HA coating with high (002) crystallographic texture (Ref 32-34). As we know, HA crystals both in vertebrate bones and in tooth enamel surface are highly oriented in the direction of their c-axis. This orientation has been proved to contribute to the chemical stability of HA coating in vivo (Ref 33). Moreover, such oriented HA coating might be useful in dentistry and orthopedics. The HA coating with (002) crystallographic texture deposited by MPS has been reported (Ref 32-34). However, the formation mechanism of crystallographic texture at (002) is still not clear. The influences of MPS parameters on the in-flight particles, splat morphology, microstructure, and phase composition of HA coatings are far from being fully understood. Phase composition and microstructure of the sprayed coatings depends upon the melting state of in-flight particles and the morphology of impinging splats. Meanwhile, the melting state of in-flight particles and the morphology of impinging splats are determined by the spray parameters. Therefore, a study on the influence of MPS parameters on the in-flight particle properties and splat types is beneficial for a good understanding of the formation mechanism of crystallographic texture in HA coating. A systematic study on the effect of spray parameter on properties of the HA coatings has important scientific significance and practical value.

In the present research, HA coatings were deposited by MPS. The effects of change in spray power and stand-off distance on HA coatings are emphasized, respectively. In order to better understand the formation mechanism of HA coatings under different spray parameters, the in-flight particles and splats were examined as well.

Materials and Methods

Hydroxyapatite powder (Medicoat, Switzerland) was employed as the raw powders for depositing the coatings. Ti-6Al-4V plates of Φ15 mm × 2.5 mm were used as the substrate. The substrate surface was grit blasted to roughen and clean the surface before deposition.

The HA coatings were sprayed by a micro-plasma spraying (WDP-1, China). A schematic diagram of micro-plasma spraying torch is shown in Fig. 1. The spray parameters for MPS are shown in Table 1. The corresponding in-flight particles were collected by liquid nitrogen. The in-flight particle velocity at different SOD was measured with the Accuraspray G3C (Tecnar, Canada). The Ti-6Al-4V substrates were ground with 400-2500 SiC paper and mirror finished with 2.5, 1 μm diamond abrasive paste before splats deposition. The polished substrates were cleaned in ultrasonic bath with ethyl alcohol and then dried in the air before spraying. From previous studies (Ref 35), a shielding plate was placed 10 mm in front of the substrate, and several holes of 1 mm in diameter were drilled on the plate to filter off individual splats (Fig. 1).

The morphologies of initial powders, in-flight particles, splats and coatings were observed by scanning electron microscopy (SEM, Hitachi, Japan), with acceleration voltage of 10 kV. The polished and polished-etched cross section of coatings was prepared before observation. Cross section of the collected powders was also ground and polished for the observation under SEM. All samples were coated with a thin gold film using gold ion sputtering system to make them electrically conductive prior to SEM observation. Coating porosity was estimated by using the ImageJ analysis software. The melting degree of in-flight particles was calculated following the approach by Khor et al. (Ref 26). Surface roughness of HA coatings were measured using a roughness sensor. The phase composition of raw powder and as-sprayed coatings was qualitatively determined through x-ray diffraction (XRD, Bruker, Germany). The operating conditions were 40 kV and 30 mA using Cu Kα radiation source. The scattering angle ranges (2θ) from 20° to 60° with a step size of 0.02°. The crystallographic texture was measured by the surface x-ray diffractometer (Bruker, Germany) with a four-circle goniometer, using Cu Kα radiation at 35 kV and 30 mA. X-ray pole figures were collected for the (002), (211) and (112) reflections of HA by varying the polar angle from 0°
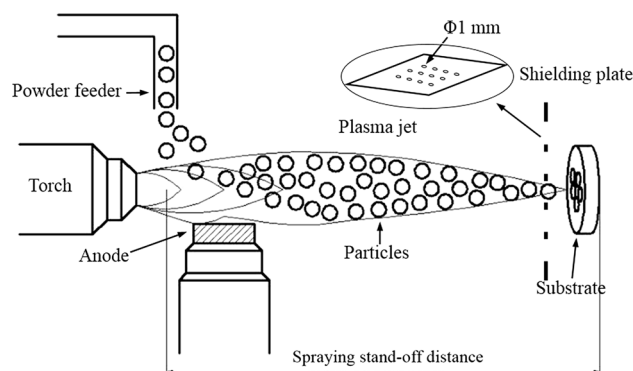

Fig. 1 Schematic diagram of micro-plasma spraying torch

Table 1 Micro-plasma spraying parameters

Sample	P1	P2	P3
Current, A	20	40	40
Voltage, V	25	25	25
Flow rate of Argon, L/min	1.3	1.3	1.3
Spraying stand-off distance, mm	60	60	110

to 85° and the azimuthal angle from 0° to 360° with step increment of 5° and a scan time of 80 s per step. The intensity is expressed in units of multiples of random distribution (MRD). The infrared thermometer (Smart sensor, China) was utilized to test the substrate temperature.

Results and Discussions

In-Flight Particles Characteristics

In-flight particles were investigated for the different spray parameter to better understand the HA coating formation mechanism in MPS. The surface morphology of raw powders and in-flight particles is shown in Fig. 2. The SEM image in Fig. 2(a) shows that the raw powders exhibit a spherical shape. Higher magnification image (Fig. 2b) shows that the HA raw powder is composed of nanoscaled rod. However, the in-flight particles morphology is very different from raw powders (Fig. 2c). There are three different morphologies observed: (1) Spherical particle with submicron grains (Fig. 2d). The possible cause of this phenomenon is that the original nanoscaled rod undergone molten or semi-molten in plasma jet and subsequently solidified or fused together. (2) Spherical particle with nanoscaled rod (Fig. 2e). The aspect ratio of nanoscaled rod was increased during spray process. There are two possible reasons for this result: the first is that the particles have undergone a lower degree of melting and the nanoscaled rod growth during spraying. The other reason for this phenomenon is that the in-flight particles may solidify before deposition due to the low plasma temperature at low spraying power or long SOD, and the crystallization was un-directional. (3) Spherical particle with smooth surface (Fig. 2f). This means that the surface of these particles was melted during spraying.

The in-flight particles size distribution is shown in Fig. 3. It can be seen that the powders sprayed with different parameters reveal different particle size distribution. The raw powders having a particles size in the range of 20-65 μm, contains 75.0 vol.% coarser particles (> 35 μm) and 25.0 vol.% small particles (20-35 μm). Compared with particle size distribution of raw powders, in-flight particles made by P1 condition are dominated by coarser particles (> 35 μm, 76.0 vol.%) (Fig. 3b). The in-flight particles sprayed using P2 condition contain 51.5 vol.% small particles (20-35 μm) (Fig. 3c). However, a direct comparison of in-flight particles size sprayed with P3 condition, indicating that size distribution is shifted toward lower values. These particles contain more small particles (20-35 μm, 75.9 vol.%) and very fine particles (< 20 μm, 7.6 vol.%). This result indicates that the in-flight particle size distribution depends on the choice of spray parameter. That in-flight particles modify their size distribution may result from the vaporization of particles surface and the disintegration of particles during spraying process. However, the in-flight temperature of HA particles is below 3500 K. It indicates that the in-flight particles were melted on the surface. There is no volatilization of P_2O_5 (Ref 36), which suggested that the in-flight particles modify their size distribution. This may result from the disintegration of particles during the spraying process. A higher heat input to the particles leads to better melting state of particles, which induced the particle disintegration with smaller particles. Figure 4 shows that the average particle velocity with different SOD. It seems that the particle velocity was slightly decreased with the longer SOD. It was assumed that the accelerated velocity of in-flight particles is constant, the flight time of particles can be described as: $t_{fly} = 2 L/v$. The average velocity of in-flight particles in P2 condition is 75.4 m/s, which is a little higher than 73.1 m/s in P3 condition. The flight time of in-flight particles was approximately 1.61 and 3.01 ms, respectively. Therefore, increasing the SOD led to the dwell time increasing and thus increased the disintegration tendency of particles. Moreover, the size distribution results confirm that more HA particles are melted at high spraying power and long spraying SOD (Fig. 3d).

The melting state of the in-flight particles can be confirmed through observing the morphology of polished cross section, which is shown in Fig. 5. The in-flight particles were collected with parameter P1, slightly 23 vol.% of the particles are completely melted and 77 vol.% of these particles are in partially melted state (Fig. 5a, b). In contrast, for the P2 condition, 91 vol.% of the particles are in a completely melted state. In these particles, the partially melted particles are rarely observed (Fig. 5c, d). In addition, in-flight particles made by P3 condition are dominated by completely melted particles (95 vol.%; Fig. 5e, f).

The final melting state of the in-flight particles is related to the spray parameter. The presence of a large number of partially melted particles in P1 condition, due to the lower spraying power is insufficient to melt the in-flight particles inside the plasma flame. On one hand, as the spraying power increases, the input heat increases, and therefore the heat that transfers from the plasma flame to the particles is
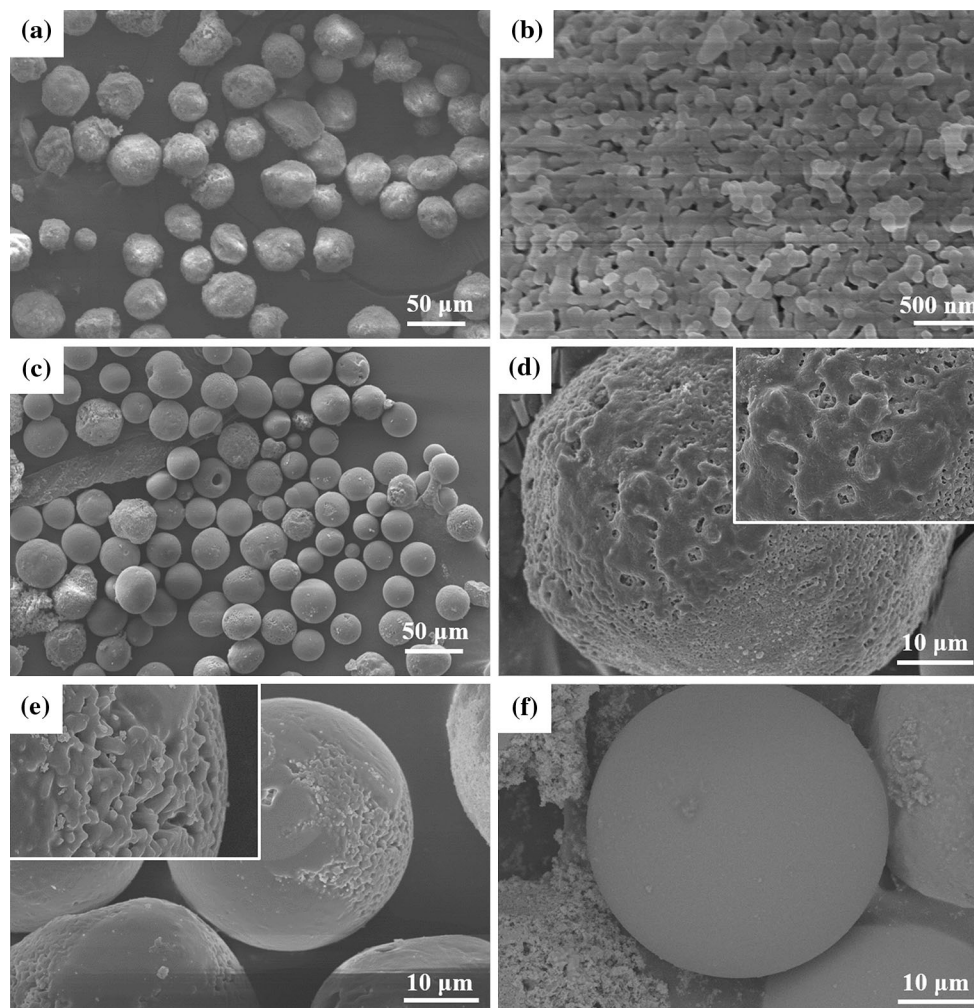
Fig. 2 Surface morphology of particles: (a, b) raw powders, (c) free in-flight particles, (d) spherical particle with submicron grains, (e) spherical particle with nanoscaled rod, and (f) spherical particle with smooth surface

sufficient to melt the particles. As a result, the particles that were collected using P2 condition contain a large number of (90%) completely melted particle. On the other hand, when the SOD increased from 60 to 110 mm, the dwell time of particles in plasma increased, therefore, there are more particles completely melting.

Splat Characteristics

Figure 6 shows the morphology of splats deposited by different spray parameters. The splat diameter results variation, which was evaluated from the splat morphology, is summarized in Fig. 7(a), (b), and (c). The average splat diameters are plotted in Fig. 6(d). The results clearly reveal the significant differences in average shapes and morphologies of the splats under different spray parameters. Splats prepared by P1 condition consist of 77 vol.% hemispherical shape splats and 23 vol.% disk shape splats (Fig. 6a). The typical range of splat diameter is from 28 to

57 μm. On the contrary, splats deposited onto the substrate by P2 condition display disk shape with some irregularity at the rim (Fig. 6b). The fraction of disk shape splat approached 100 vol.%. The diameter of the splats is in the range of 31-105 μm. Whereas, the splats deposited under P3 condition exhibit splashed shape (Fig. 6c). The fraction of splashed shape splats is near 43 vol.%. The diameter of the splat is in the range of 60-145 μm. In addition, 37 vol. % hemispherical shape splats of 25-38 μm diameter and 20 vol.% smaller disk shape splats (39-50 μm), which are generally formed by small particles, can also be seen (Fig. 3c). The average splat diameters are plotted in Fig. 7 (d).

The different splat morphologies are formed under different spray parameters with the results shown in Fig. 6. The influencing factor can be found in the melting degree of the individual particles and the substrate temperature. At the P1 condition, there are a large number of particles that are in partially melted state. These particles flatten to
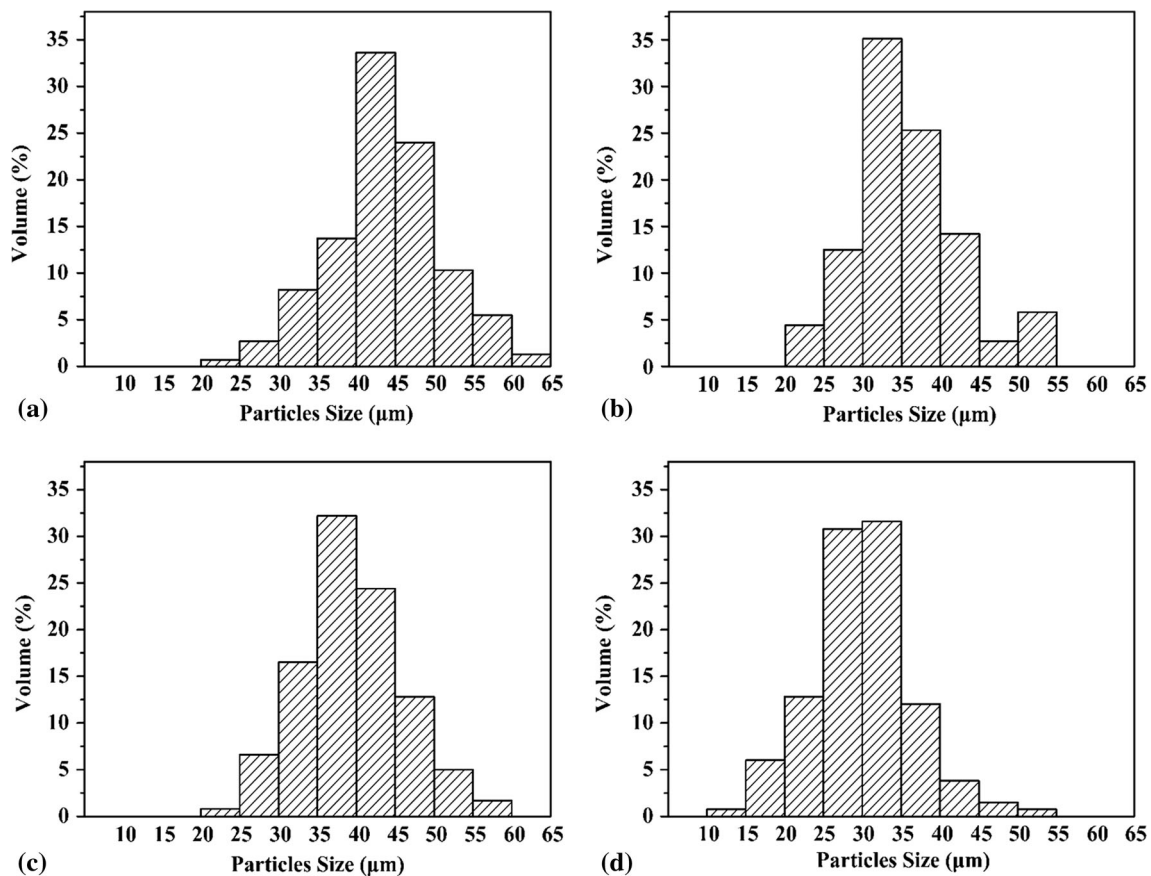
Fig. 3 In-flight particles size distribution: (a) raw powders, (b) P1, (c) P2, and (d) P3
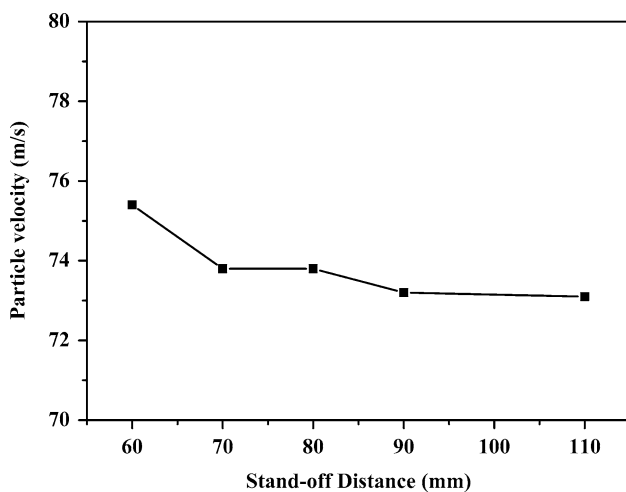

Fig. 4 Average of in-flight particle velocity for the different SOD

The plasma jet diameter is 2-3 mm and sprayed spot size is 5-7 mm. It means that the plasma jet is concentrated on the substrate. In shorter SOD, the heat from the plasma jet increased, which increased the substrate temperature. For these reasons, the local temperature of substrate can reach up to 200 °C. Completely melted particles that deposited onto heated substrate are able to spread out and developed into predominantly disk shape splats or limited splashing at its rim. However, as the SOD increased from 60 to 110 mm, the substrate is further from the plasma jet, and the temperature of substrate is greatly decreased (40 °C), which lead to the splat on the polished substrate changed from disk shape to splashed shape. For instance, smaller particles cool down more quickly during flight, which resulted in the formation of hemispherical shape splats and smaller disk shape splats.

Coatings Characteristics

Figure 8 shows the XRD patterns of the HA coatings sprayed at different parameters. The XRD spectrum of raw powder shows that all diffraction peaks and relative intensities are assigned to standard HA powder pattern (JCPDS 09-0432) and the raw powder exhibits random

substrate are not able to spread out and thus exhibiting hemispherical shape. Meanwhile, some completely melted particles impinge on the substrate and show disk shape. In this study, MPS provides a concentrate plasma torch and stable laminar plasma flow, which results in a steady stable plasma flow impinging upon the substrate (Ref 37).
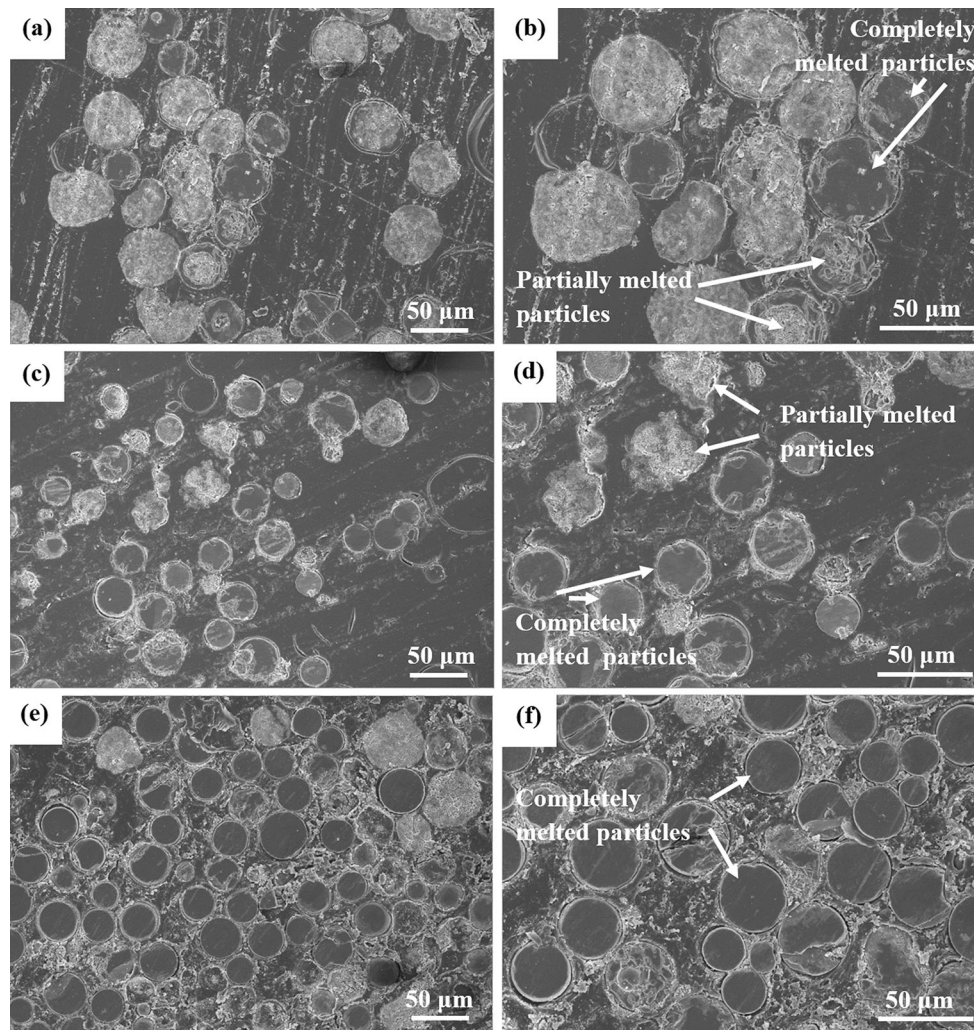
Fig. 5 SEM morphology of the cross section of in-flight particles: (a, b) P1, (c, d) P2, and (e, f) P3

crystal orientation (Fig. 8a). In contrast to HA raw powders, TTCP, α-TCP, β-TCP and ACP are observed in HA coatings, and the phase CaO cannot be identified in the patterns. It is noted that the phase composition of the P1 coating is similar to that of the raw powders (Fig. 8b). The highest HA content amounts to over 93.3%. For coating sprayed at P2, the highest HA content is over 86%. Specifically, the (002) peak in the P2 coating appears markedly higher than other HA peaks. Such XRD patterns indicate that a recrystallization of the HA phase occurred during the deposition, with a preferred orientation of (002) crystallographic planes (Fig. 8c). XRD pole figures are shown in Fig. 8(e). Different colors represent different value of intensity. The pole figures for the P2 coating show random distribution of HA (211) and (112) poles. The strongest point of pole figures is at the center of (002) pole figure. It can be seen from the x-ray pole figure that the maximum intensities of (002) pole figure is 6.95. This indicates that P2 coating shows (002) crystallographic

texture. As the SOD increased from 60 to 110 mm, the amorphous hump becomes significant (Fig. 8d). The highest ACP content amounts to 50%, and the lowest HA content is only 30%. In addition, the α-TCP of P1 coating amounts to 3.2% (Fig. 8b). Compared with the P1 coating, the highest α-TCP content in the P2 coating is over 14% (Fig. 8c). For the P3 coating, the α-TCP increases to 20% (Fig. 8d). Moreover, it is also noted that trace amounts of TTCP are observed in the P1 coating (Fig. 8b).

In this study, at the P1 condition, the lower spraying power is insufficient to melt all the HA powders during spraying. Only the smaller powder particles were melted, and the large particles were only partially melted (Fig. 5a, b). However, the raw powders mainly consist of large size particles (Fig. 3a), so that the morphology of the P1 coating was dominated by partially melted particles (Fig. 5a, b). The unmelted part within the in-flight particles remained in the specimen. The presence of a greater amount of crystalline HA and a small amount of phase decomposition
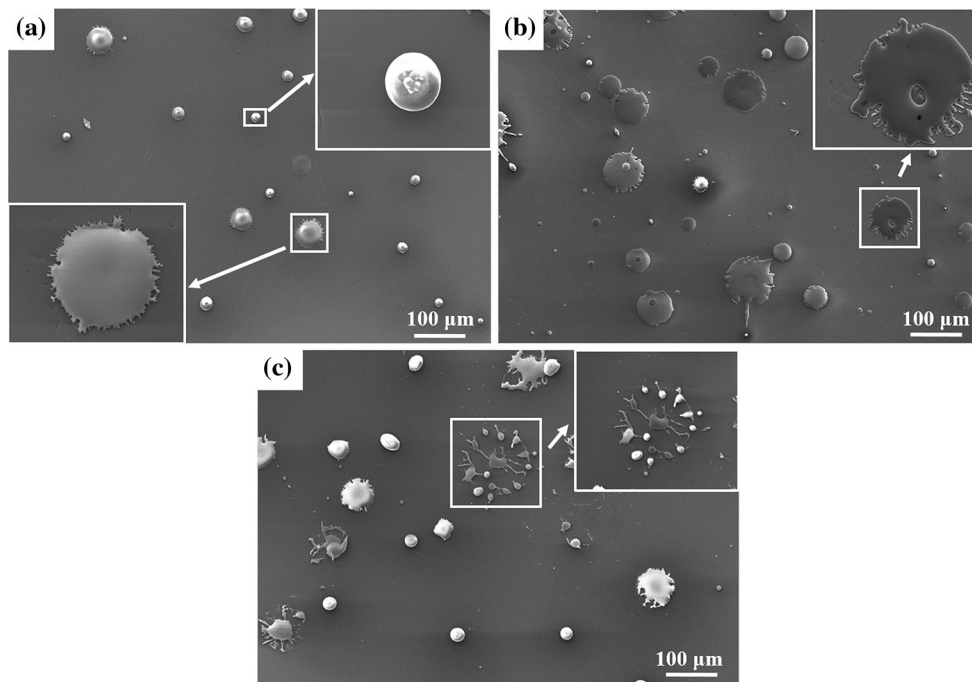
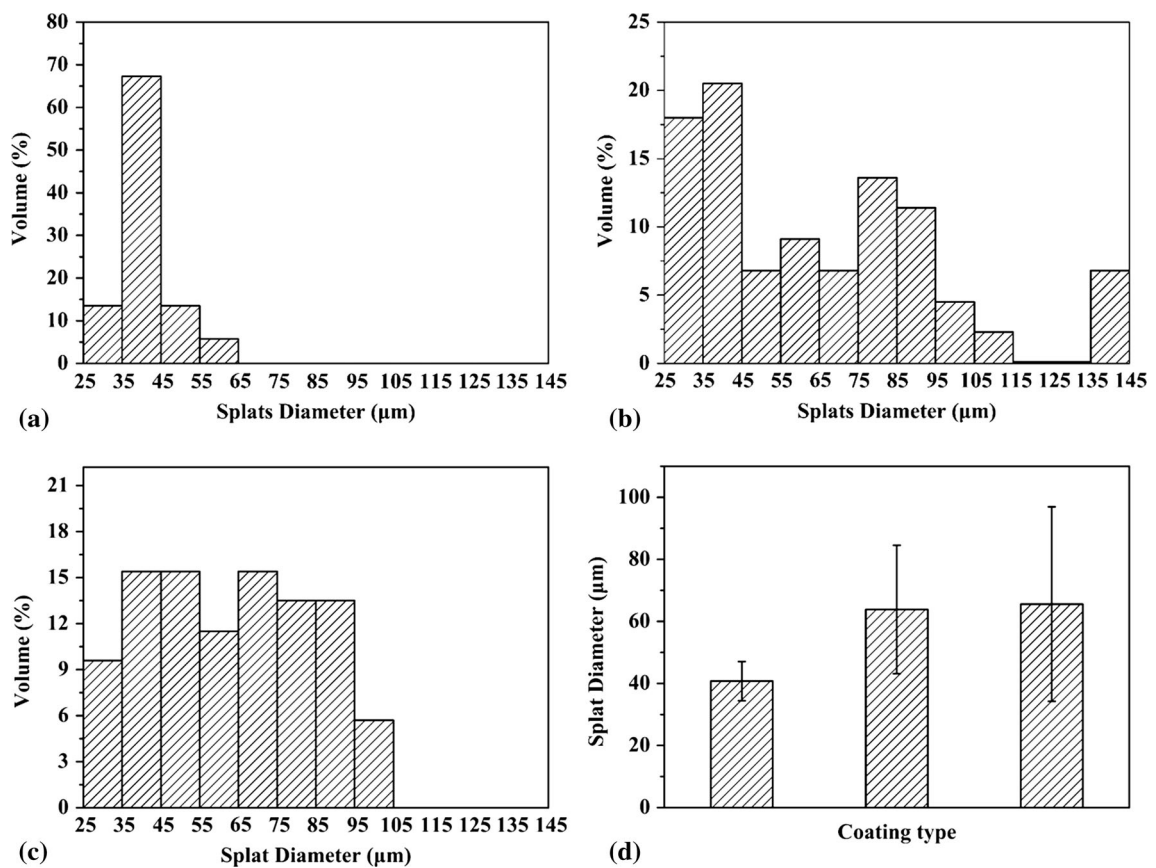**Fig. 6** Morphologies of HA splats for different parameters: (a) P1, (b) P2, and (c) P3

Fig. 7 Splat diameter for different parameters: (a) P1, (b) P2, (c) P3, and (d) average diameter
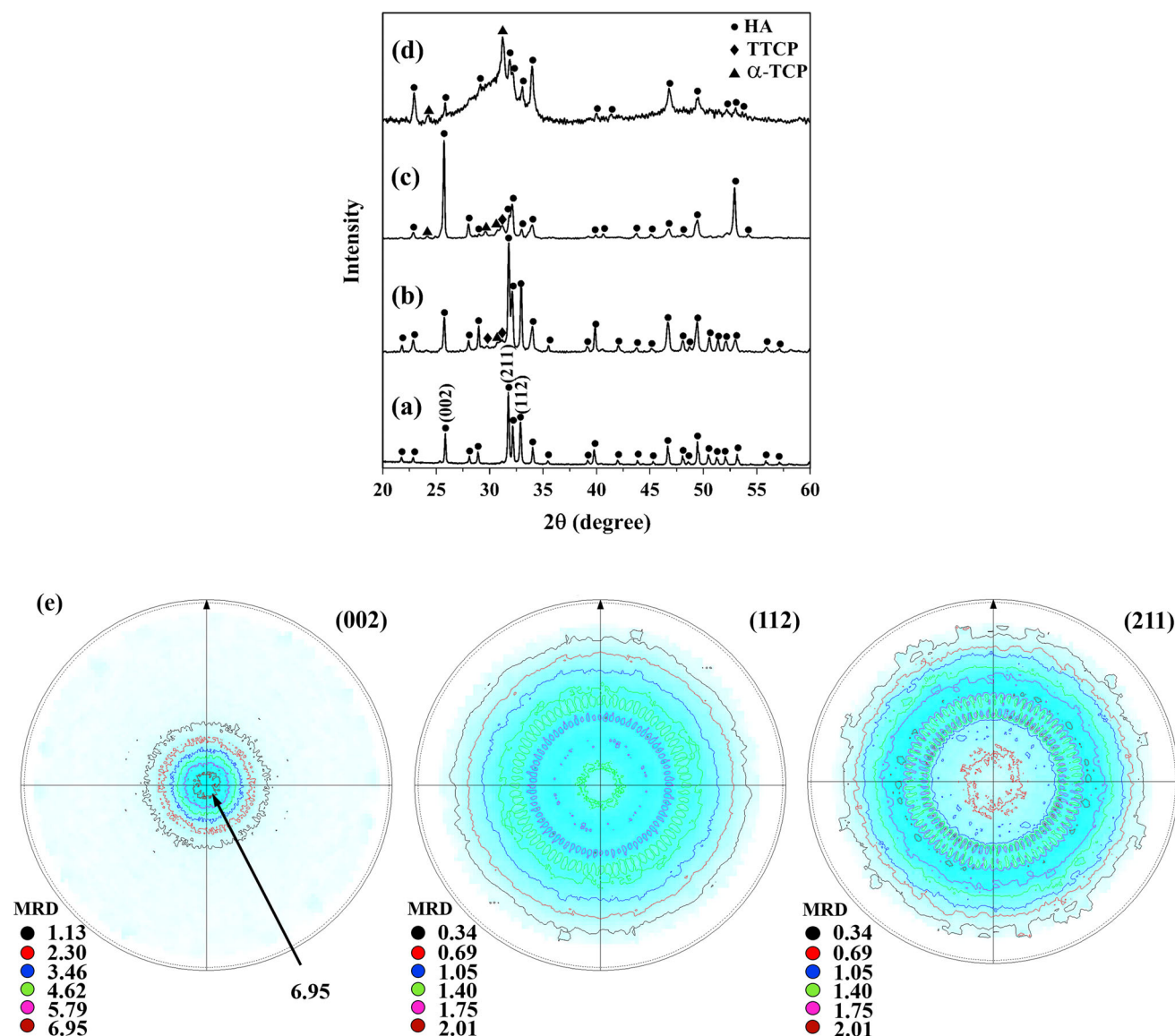
Fig. 8 XRD pattern of as-sprayed HA coatings showing the influence of spray parameter on phase composition of resultant coatings: (a) raw powder, (b) P1 coating, (c) P2 coating, (d) P3 coating, and (e) pole figures

(TTCP, α-TCP and β-TCP) within the partially melted particle is beneficial to high crystallinity of final coating. The cooling rate of splat ($\dot{T}$) can be described as $\dot{T} = \lambda\,(T_1 - T_s)/c_\rho \rho d^2$ (Ref 38), where T_1 is the surface temperature of in-flight particles, T_s is the substrate temperature, λ is thermal conductivity, c_ρ is the thermal capacity, d is the splat thickness, and ρ refers to density of deposition material. At the P2 condition, the increased content of α-TCP was formed in the P2 coating, which indicates large quantities of phase transformation during the spraying due to more particles melting (Fig. 5c, d). The completely melted particle deposited to substrate show disk shape (Fig. 6b). The average thickness of disk shape splat is in the range of 2-6 μm, which is much higher than splashed shape

splat (1 μm). The surface average temperature of in-flight particles in P2 condition is 2385.04 K, a little higher than 2265.09 K in P3 condition. In addition, the heat input from flame and the incoming droplets increased, which increased the substrate temperature to 300 °C. However, the substrate temperature greatly decreased to 100 °C as the heat accumulation from the plasma flame was decreased under long SOD. These parameter values are shown in Table 2. After calculation, the cooling rates of the disk shape splat deposited by P2 and splashed shape splat deposited by P3 coating approximately 1.01×10^8 and 1.69×10^9 K/s. It has been reported that the {0 0 0 1} surface is of the lowest surface energy among all orientations in crystalline HA (Ref 35). From this point of view, HA films may tend to

Table 2 Thermo-physical constants and measurements of HA used in calculation

Parameters	Value	References
Thermal conductivity (λ), W/m-K	0.72 (283 K)	Ref 36
	2.16 (1352 K)	
Thermal capacity (c_ρ), J/Kg-K	766 (293-1300 K)	Ref 39
Density (ρ), Kg/m^3	3156	Ref 40
Surface temperature of in-flight particles (T_l)/P2, K	2385.04	…
Surface temperature of in-flight particles (T_l)/P3, K	2265.09	…
Substrate temperature (T_s)/P2, °C	300	…
Substrate temperature (T_s)/P3, °C	100	…
Splat thickness/P2, μm	2-6	…
Splat thickness/P3, μm	< 1	…

grow along the c-axis with a (002) orientation to minimize the surface energy (Ref 41). For this reasons, low cooling rate of P2 disk shape splats lead to HA grains along (002) within P2 coating. Compared with disk shape splat, splashed shape splat had a higher cooling rate. Moreover, longer dwell time of in-flight particles in plasma flame during P3 coating caused phase decomposition additionally. These two factors lead to the higher ACP and TCP in P3 coating.

Surface morphology of HA coatings is shown in Fig. 9. The morphology of P1 coating is dominated by partially melted particles and some flatten splats (Fig. 9a, b). A large number of pores (5%) are observed for P1 coating (Fig. 9a, b). This surface morphology is consistent with the previous in-flight particles results. The surface of the P2 coating is dominated by well-flattened splats (Fig. 9b, c). In contrary to P1 coating, P3 coating contains a lot of spherical particles and the quantity of pores increased (Fig. 9e, f). This was supported by in-flight particles and splats results that particles were collected using P3 condition show more fine spherical particles and hemispherical shape splats. The surface morphology of HA coatings shows a good correlation to the particle melted state and the splat type. In addition, cracks can also be observed in all coatings due to the formation of stresses during spraying process. The final coating is built by the numerous single splats, and the coating morphologies are determined by the flattening of splats. Partially melted particles were larger and just melted on the surface. These particles impact the substrate, which leads to smaller splat diameter (Fig. 6a). As a result, the overall result is a rougher coating (Ra = 11.30 μm). P2 coating showed that the in-flight particles melted enough to form a dense surface, the number of observed spherical particles were less in comparison to P1 coating. Therefore, the P2 coating exhibited smoother surface morphology and lower roughness value (Ra = 5.63 μm). The average diameter of the splats for the P2 and P3 is higher than that in P1 condition. However, the P3 coating exhibited a relatively rough surface morphology (Ra = 9.72 μm) and high porosity due to the small splat diameter of the smaller particles (Fig. 7c).

The cross-sectional morphology of the coatings is shown in Fig. 10. In the polished cross section of P1 coating, a large number of pores (20%) are distributed throughout the coating (Fig. 10a). This can be attributed to the impingement of partially melted particles on the substrate, which showed hemispherical shape (Fig. 6a) and their embedding in the coating therefore leads to the formation of a loose composed with high porosity. A smaller diameter of the hemispherical splats increases and decreases the contacts of touching each other, the amount of pores increases. On the contrary, P2 (8% porosity) and P3 (4% porosity) exhibit a dense structure without obvious spherical particles, splats' boundary and lamellar interfaces (Fig. 10c, e). The particles are very well melted under the P2 and P3 condition (Fig. 5c, d, e, and f). The closely packed disk splats and splashed splats make the whole coating to obtain a compact structure with dense structure. Consequently, the porosity is directly influenced by the particle splat shape. Chemically etched cross-sectional morphology of P1 coating shows that there are a relatively high number of partially melted particles (Fig. 10b). The microstructure of this coating is not the characteristic lamellar structure. It is noted that the HA grains located in unmelted part are much larger than the size of those nanoscaled rod in raw powder (Fig. 2b) and this indicates the growth of the grains during spraying. This result is consistent with the previous in-flight particles surface morphology (Fig. 2e). The relative increased grain size located in the unmelted part might not be favorable to improve mechanical properties and bioactivity. However, P2 coating after chemical etching shows typical lamellar structure with columnar grains and it does not have any partially melted particles (Fig. 10d). These columnar grains grew along deposition direction, which corresponds to the XRD results that showed a strong (002) crystallographic texture (Fig. 8c). Because of the higher melting degree of in-flight particles, the complete particles flatten and spreads
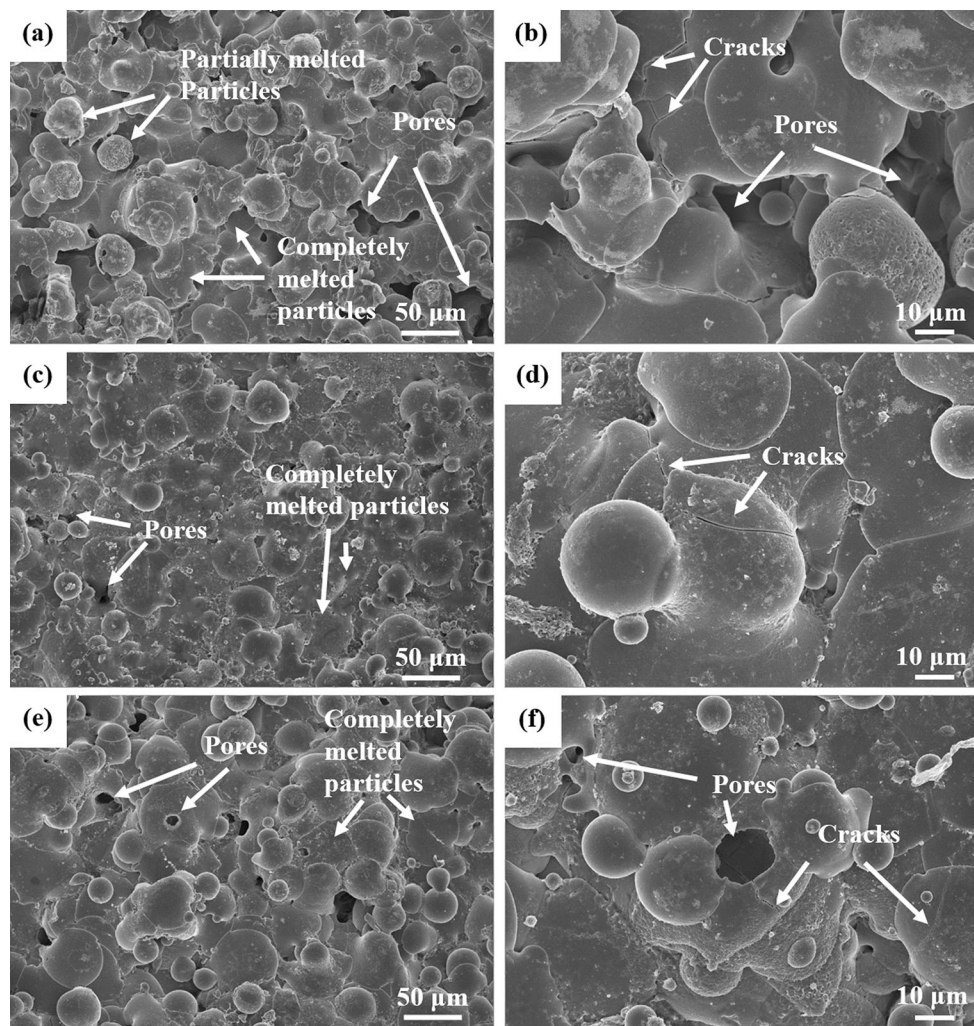
Fig. 9 Surface morphology of the HA coatings: (a, b) P1 coating, (c, d) P2 coating, and (e, f) P3 coating

too much higher degree than in the case of P1 condition. This high degree of flattening leads to the increase in the splats diameter and reduction in lamellae thickness (Fig. 7b, d), which developed non-splashed and predominantly disk shape splats or limited splashing at its rim (Fig. 6b). These shape splats constitute layers in the coating and these layers in turn create the lamellar structure of the coating (Fig. 10d). The heat flux of the disk shape splats was perpendicular to the substrate surface (Ref 42), hence promoting the (002) crystal growth along deposition direction during MPS. On the other hand, when the spraying power increased, the substrate temperature was improved. Under such condition, the splat solidification occurred at a slow cooling rate, and the columnar grains have enough time to grow along the direction of heat dissipation. Indeed, higher substrate temperature is beneficial to obtain disk shape splats, which provided a heat flow perpendicular to the surface of the substrate. Meanwhile, the heat input form plasma and successive splats provided a

lower cooling rate. For these two reasons, the high columnar crystalline HA preferred to grow within the P2 coating. Moreover, SEM observations clearly show that the columnar grains did not go beyond the boundary of the HA splats. It is considered that the ACP or TCP shell can be formed from the bottom of splat when contacting the previously deposited splats. ACP or TCP may dissolve easily in the dilute hydrochloric acid solution. On the contrary, the columnar with high chemically stable remains in the coating. Our results are consistent with the previous finding (Ref 43). The columnar structure might have a beneficial effect on biocompatibility osteogenic differentiation of implants.

However, there are no obvious columnar grains in the chemical etched cross section of the P3 coating (Fig. 10f). The high-magnification SEM showed that a small number of splats with columnar grains were present in P3 coating. Two aspects are concerned with this phenomenon. On one hand, there are more splashed shape splats observed
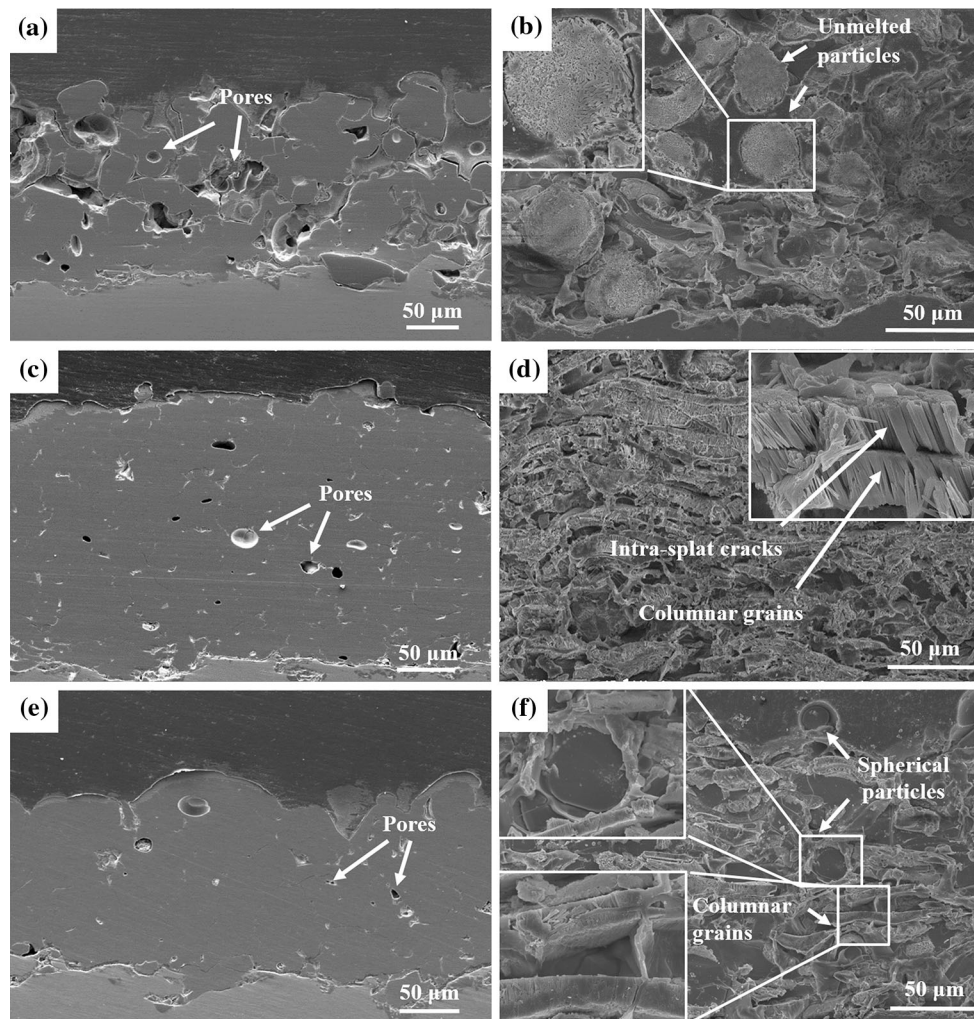
Fig. 10 Cross-sectional morphology of HA coatings: (a) P1 coating, (b) P2 coating, (c) P3 coating, (d) chemically etched P1 coating, (e) chemically etched P2 coating, and (f) chemically etched P3 coating

(Fig. 6c); however, splashed shape splats are not observed in the P2 coating (Fig. 10b). The cooling rate of splashed shape splats is higher than that of the disk shape splats, leading to the formation of ACP and TCP within HA coating. The high cooling rate of splats is not beneficial to the formation of columnar. On the other hand, in this coating, a small number of droplets impinge on the substrate without splashing (Fig. 6c). These splats solidification occurred at slow cooling rate and contributed to the formation of columnar grains (Fig. 10d). Columnar grains could not form in hemispherical shape splat under a unidirectional heat flow before deposited. For these reasons, the number of splats with columnar grains is significantly reduced compared with P2 coating, which results in the fact that the (002) crystallographic texture is not seen from XRD analysis (Fig. 8d). Therefore, it is confirmed that the splat morphology and the cooling rate would have a crucial effect on the coating structure. The splat morphology is influenced by melting state and substrate temperature. The cooling rate is determined by the splat shape and the heat input of plasma.

Conclusions

Bioactive HA coatings were deposited onto Ti-6Al-4V substrates by MPS using different spray parameters. The influence of spray parameters on the coating phase composition and microstructure was investigated. The in-flight particles and single splats were collected to establish the relationship between coating structure with the in-flight particle melting state and splat types.

The following conclusions are obtained:

1. HA coatings sprayed at low spraying power and SOD exhibit high crystallinity and porosity is attributed to the presence of partially melted particles. High

crystallinity HA coatings with (002) crystallographic texture could be deposited due to the complete melting of the in-flight particles and low cooling rate of the disk shape splats under higher spraying power and shorter SOD. However, splashed shape splats with relative high cooling can be provided by increasing SOD, which leads to the formation of ACP.

2. Orderly distributed columnar structure was formed in HA coating deposited by MPS, correspond to an extreme strong (002) crystallographic texture. The formation of (002) crystallographic texture requires two conditions: (1) the in-flight particles must be completely melted before hitting to the substrate, (2) the substrate must have higher temperature in order to fabricated splat with disk shape after deformation.

3. MPS is feasible to deposit textured HA coating without complex process. It may be possible applying to optimize crystallographic texture of HA during plasma spraying.

References

1. M.N. Rahaman, W. Xiao, Y. Liu, and B. Sonny Bal, Osteoconductive and Osteoinductive Implants Composed of Hollow Hydroxyapatite Microspheres, in *Advances in Bioceramics and Porous Ceramics VII: 38th International Conference on Advanced Ceramics and Composites*, eds. by R. Narayan, and P. Colombop, 27–31 Jan 2014(Daytona Beach, Florida) (American Ceramic Society and ACerS's Engineering Ceramics Division, 2014)

2. B. Locardi, U.E. Pazzaglia, C. Gabbi, and B. Profilo, Thermal Behaviour of Hydroxyapatite Intended for Medical Applications, *Biomaterials*, 1993, **14**(6), p 437-441

3. S.V. Dorozhkin, Calcium Orthophosphate-Based Biocomposites and Hybrid Biomaterials, *J. Mater. Sci.*, 2009, **44**(9), p 2343-2387

4. Y.C. Yang and C.Y. Yang, Mechanical and Histological, Evaluation of a Plasma Sprayed Hydroxyapatite Coating on a Titanium Bond Coat, *Ceram. Int.*, 2003, **29**(6), p 6509-6516

5. R.B. Heimann, Structure, Properties, and Biomedical Performance of Osteoconductive Bioceramic Coatings, *Surf. Coat. Technol.*, 2013, **233**, p 27-28

6. M.F. Hasan, J. Wang, and C. Berndt, Evaluation of the Mechanical Properties of Plasma Sprayed Hydroxyapatite Coatings, *Appl. Surf. Sci.*, 2014, **303**, p 155-162

7. H.P. Li, Q.Y. Zhao, B. Li, J.L. Kang, Z.Y. Yu, Y.X. Li, X.Q. Song, C.Y. Liang, and H.S. Wang, Fabrication and Properties of Carbon Nanotube-Reinforced Hydroxyapatite Composites by a Double in Situ Synthesis Process, *Carbon*, 2016, **101**, p 159-167

8. V. Kosma, T. Tsoufis, T. Koliou, A. Kazantzis, K. Beltsios, J.T. M. De Hosson, and D. Gournis, Fibrous Hydroxyapatite-Carbon Nanotube Composites by Chemical Vapor Deposition. In Situ Fabrication, Structural and Morphological Characterization, *Mater. Sci. Eng. B*, 2013, **178**(7), p 457-464

9. E. Mohseni, E. Zalnezhad, A.R. Bushroa, A.M. Hamouda, B.T. Goh, and G.H. Yoon, Ti/TiN/HA Coating on Ti-6Al-4V for Biomedical Applications, *Ceram. Int.*, 2015, **41**(10), p 14447-14457

10. A. Rabiei, B. Thomas, C. Jin, R. Narayan, J. Cuomo, Y. Yang, and J.L. Ong, A Study on Functionally Graded HA Coatings Processed Using Ion Beam Assisted Deposition with in Situ Heat Treatment, *Surf. Coat. Technol.*, 2006, **200**(20–21), p 6111-6116

11. I.-S. Lee, B.H. Zhao, G.-H. Lee, S.-H. Choi, and S.-M. Chung, Industrial Application of Ion Beam Assisted Deposition on Medical Implants, *Surf. Coat. Technol.*, 2007, **201**(9–11), p 5132-5137

12. C.X. Wang, Z.Q. Chen, L.M. Guan, M. Wang, Z.Y. Liu, and P.L. Wang, Fabrication and Characterization of Graded Calcium Phosphate Coatings Produced by Ion Beam Sputtering/Mixing Deposition, *Nucl. Instrum. Methods B*, 2001, **179**(3), p 365-372

13. H.-C. Choe, W.-G. Kim, and Y.-H. Jeong, Surface Characteristics of HA Coated Ti-30Ta-xZr and Ti-30Nb-xZr Alloys after Nanotube Formation, *Surf. Coat. Technol.*, 2010, **205**, p s305-s311

14. Y.-H. Jeong, H.-C. Choe, and S.-W. Eun, Hydroxyapatite Coating on the Ti-35Nb-xZr Alloy by Electron Beam-Physical Vapor Deposition, *Thin Solid Films*, 2011, **519**(20), p 7050-7056

15. H.-C. Choe, Photofunctionalization of EB-PVD HA-Coated Nano-pore Surface of Ti-30Nb-xZr Alloy for Dental Implants, *Surf. Coat. Technol.*, 2013, **228**, p s470-s476

16. H. Maleki-Ghaleh, V. Khalili, J. Khalil-Allafi, and M. Javidi, Hydroxyapatite Coating on NiTi Shape Memory Alloy by Electrophoretic Deposition Process, *Surf. Coat. Technol.*, 2012, **208**, p 57-63

17. M. Javidi, S. Javadpour, M.E. Bahrololoom, and J. Ma, Electrophoretic Deposition of Natural Hydroxyapatite on Medical Grade 316 L Stainless Steel, *Mater. Sci. Eng. C*, 2008, **28**(8), p 1509-1515

18. E. Karimi, J. Khalil-Allafi, and V. Khalili, Electrophoretic Deposition of Double-Layer HA/Al Composite Coating on NiTi, *Mater. Sci. Eng. C*, 2016, **58**, p 882-890

19. L. Besra and M. Liu, A Review on Fundamentals and Applications of Electrophoretic Deposition (EPD), *Prog. Mater. Sci.*, 2007, **52**(1), p 1-61

20. J.C. Huang, Y.J. Ni, and Z.C. Wang, Preparation of Hydroxyapatite Functionally Gradient Coating on Titanium Substrate using a Combination of Electrophoretic Deposition and Reaction Bonding Process, *Surf. Coat. Technol.*, 2010, **204**(21–22), p 3387-3392

21. D.G. Wang, C.Z. Chen, J. Ma, and T. He, Microstructure Evolution of Sol–Gel HA Films, *Appl. Surf. Sci.*, 2011, **257**(7), p 2592-2598

22. H.W. Kim, Y.H. Koh, L.H. Li, S. Lee, and H.E. Kim, Hydroxyapatite Coating on Titanium Substrate with Titania Buffer Layer Processed by Sol–Gel Method, *Biomaterials*, 2004, **25**(13), p 2533-2538

23. X.L. Zeng, J.F. Li, S.H. Yang, Q.X. Zheng, and Z.W. Zou, Preparation of Artificial Canine Femoral Stem with HA-Ti Ladder-Type Coating on Plasma-Sprayed Pure Ti Substrate and its Performance Evaluation, *Appl. Surf. Sci.*, 2012, **258**(10), p 4489-4496

24. H.C. Gledhill, I.G. Turner, and C. Doyle, In Vivo Fatigue Behaviour of Vacuum Plasma and Detonation Gun Sprayed Hydroxyapatite Coatings, *Biomaterials*, 2001, **22**(11), p 1233-1240

25. H.C. Gledhill, I.G. Turner, and C. Doyle, Direct Morphological Comparison of Vacuum Plasma Sprayed and Detonation Gun Sprayed Hydroxyapatite Coatings for Orthopaedic Applications, *Biomaterials*, 1999, **20**(4), p 315-322

26. K.A. Khor, H. Li, and P. Cheang, Significance of Melt-Fraction in HVOF Sprayed Hydroxyapatite Particles, Splats and Coatings, *Biomaterials*, 2004, **25**(7–8), p 1177-1186

27. K.A. Khor, H. Li, P. Cheang, and S.Y. Boey, In Vitro Behavior of HVOF Sprayed Calcium Phosphate Splats and Coatings, *Biomaterials*, 2003, **24**(5), p 723-735

28. H. Li, K.A. Khor, and P. Cheang, Young's Modulus and Fracture Toughness Determination of High Velocity Oxy-Fuel-Sprayed Bioceramic Coatings, *Surf. Coat. Technol.*, 2002, **155**(1), p 21-32

29. V. Deram, C. Minichiello, R.N. Vannier, A.L. Maguer, L. Pawlowski, and D. Murano, Microstructural Characterizations of Plasma Sprayed Hydroxyapatite Coatings, *Surf. Coat. Technol.*, 2003, **166**(2–3), p 153-159

30. L.M. Sun, C.C. Berndt, and C.P. Grey, Phase, Structure and Microstructural Investigation of Plasma Sprayed Hydroxyapatite Coatings, *Mater. Sci. Eng. A*, 2003, **360**(1–2), p 70-84

31. S. Vahabzadeh, M. Roy, A. Bandyopadhyay, and S. Bose, Phase Stability and Biological Property Evaluation of Plasma Sprayed Hydroxyapatite Coatings for Orthopedic and Dental Applications, *Acta Biomater.*, 2015, **17**, p 47-55

32. Y.M. Wang, X.M. Liu, T.T. Fan, Z. Tan, Z. Zhou, and D.Y. He, In Vitro Evaluation of Hydroxyapatite Coating with (002) Crystallographic Texture Deposited by Micro-plasma Spraying, *Mater. Sci. Eng. C*, 2017, **75**, p 596-601

33. Y.M. Wang, T.T. Fan, Z. Zhou, and D.Y. He, Hydroxyapatite Coating with Strong (002) Crystallographic Texture Deposited by Micro-plasma Spraying, *Mater. Lett.*, 2016, **185**, p 484-487

34. L. Zhao, K. Bobzin, F. Ernst, J. Zwick, and E. Lugscheider, Study on the Influence of Plasma Spray Processes and Spray Parameter on the Structure and Crystallinity of Hydroxyapatite Coatings, *Materialwiss*, 2006, **37**(6), p 516-520

35. M.R.T. Filgueiras, D. Mkhonto, and N.H. de Leeuw, Computer Simulations of the Adsorption of Citric Acid at Hydroxyapatite Surfaces, *J. Cryst. Growth*, 2006, **294**(1), p 60-68

36. S. Dyshlovenko, B. Pateyron, L. Pawlowski, and D. Murano, Numerical Simulation of Hydroxyapatite Powder Behaviour in Plasma Jet, *Surf. Coat. Technol.*, 2004, **179**(1), p 110-117

37. E. Lugscheider, K. Bobzin, L. Zhao, and J. Zwick, Assessment of the Microplasma Spraying Process for Coating Application, *Adv. Eng. Mater.*, 2006, **8**(7), p 635-639

38. Y. Wang, Y. Bai, J.J. Tang, Y.H. Wang, K. Liu, S.W. Guo, and Z.H. Han, A transmission Electron Microscopy Study of the Microstructure and Interface of Zirconia-based Thermal Barrier Coatings, *J. Alloys Compd.*, 2015, **619**, p 820-825

39. T.W. Clyne and Y.C. Tsui, The Effect of Intermediate Layers on Residual Stress Distributions and Debonding of Sprayed Thermal Barrier Coatings, *FGM*, 1995, **94**, p 129-136

40. K.M. Kh and K.M. Kh, *Handbook of Thermodynamic Constants of Inorganic and Organic Compounds*, Ann Arbor-Humphrey Science Publishers, Ann Arbor, 1970

41. S. Serrano-Zabaleta, M.A. Laguna-Bercero, L. Ortega-San-Martín, and A. Larrea, Orientation Relationships and Interfaces in Directionally Solidified Eutectics for Solid Oxide Fuel Cell Anodes, *J. Eur. Ceram. Soc.*, 2014, **34**(9), p 2123-2132

42. I. Iordanova and K.S. Forcey, Texture and Residual Stresses in Thermally Sprayed Coatings, *Surf. Coat. Technol.*, 1997, **91**(3), p 174-182

43. M. Inagaki and T. Kameyama, Phase Transformation of Plasma-sprayed Hydroxyapatite Coating with Preferred Crystalline Orientation, *Biamaterials*, 2007, **28**(19), p 2923-2931